Theoretical and Applied Climatology
https://doi.org/10.1007/s00704-020-03185-5

ORIGINAL PAPER

Application of MJO dynamics-oriented diagnostics to CMIP5 models

Juan Li[1] · Ying Yang[1] · Zhiwei Zhu[1]

Received: 15 January 2020 / Accepted: 15 March 2020

Abstract
Realistic simulation of Madden–Julian Oscillation (MJO) propagation in coupled global climate models remains a common problem. In this study, the ability of 20 coupled models from Coupled Model Intercomparison Project Phase 5 (CMIP5) in simulating MJO is examined using dynamics-oriented diagnostics. The diagnostics focus on dynamic and thermodynamic structures of MJOs on three dimensions, which help to identify the shortcomings of models and evaluate whether they could reproduce MJO for the right reason. According to the simulation performance of the eastward propagation of MJO, the "good" models and "poor" models are detected. The dynamics-oriented diagnostics are further applied to the good models, poor models, and all models to establish a linkage between MJO simulation skill and their dynamic/thermodynamic structures. Results show that the simulations of good models have the following common features: (1) a horizontal zonal structural asymmetry in low-level zonal wind, upper-level diabatic heating and divergence; (2) a preceding eastward propagation of boundary layer moisture convergence; and (3) a rearward-tilted vertical structure of diabatic heating, equivalent potential temperature and available potential energy generation. The poor models that fail to capture these three-dimensional structures do not reproduce the eastward propagation of MJO. More than half of these 20 CMIP5 models still have difficulties in simulating these dynamic/thermodynamic structures.

1 Introduction

Madden–Julian Oscillation (MJO) is the major mode of tropical variability with a periodicity of 20–70 days. MJO has the ability to influence the formation of tropical cyclone activity (Hall et al. 2001; Ho et al. 2006; Jiang et al. 2012), monsoonal circulation, and rainfall by changing moisture during its different phases (Bhatla et al. 2017; Singh et al. 1992; Stewart 2009; Wheeler et al. 2009), extreme weather events (Christophe 2008; Jones 2000; Zhou et al. 2012), and the mid–high-latitude climate through inducing atmospheric teleconnection (Ferranti et al. 1990; Hai et al. 2009; Wang and Ding 1992; Yoo et al. 2012; Yang et al. 2020). In addition, MJO is the major source of global predictability on intraseasonal timescales. Thus, in general circulation models (GCMs), realistic simulation of MJO is one of the key factors for skillful prediction of a wide variety of climate phenomena.

Although great efforts have been made in improving MJO simulations, simulating it realistically has long been a great challenge. Typical MJO errors in GCMs include a weak amplitude, shorter period for MJO decay, small spatial extent of convection, and lack of coherent eastward propagation (Jiang et al. 2015; Kim et al. 2009; Liu et al. 2009; Slingo et al. 1999; Sperber 2003; Sperber 2004). To evaluate and track the progress of coupled GCM (CGCM) simulations of MJO, the MJO Working Group funded by the US Climate Variability and Predictability Program (CLIVAR) developed a diagnostics package (Waliser et al. 2009) in a standardized manner. Using these diagnostics, Kim et al. (2009) analyzed eight climate models and indicated that the timescale of MJO decay for all models is shorter than observed. Liu et al. (2009) showed that the simulated tropical intraseasonal variability is unrealistic, and the simulated MJO has a standing structure, although about one-third of the CMIP5 models captured the 30- to 70-day spectral peak of MJO (Hung et al. 2013). Jiang et al. (2015) revealed that only about a quarter of 24 GCM simulations can simulate the eastward propagation well. Most CMIP5 models show weak MJO amplitude (Ahn et al. 2017).

The diagnostics developed by the CLIVAR MJO group provide a comprehensive evaluation of the behavior of MJO,

✉ Zhiwei Zhu
zwz@nuist.edu.cn

[1] Key Laboratory of Meteorological Disaster, Ministry of Education (KLME)/Joint International Research Laboratory of Climate and Environment Change (ILCEC)/Collaborative Innovation Center on Forecast and Evaluation of Meteorological Disasters (CIC-FEMD), Nanjing University of Information Science and Technology, 219 Ningliu Road, Meteorology Bldg., Nanjing 210044, China

Published online: 09 May 2020

but only reflect the MJO's statistical properties. These diagnostics are useful, but some of them are hard to quantitatively measure the skill of models. From a dynamical standpoint, Wang et al. (2018) developed a suite of complementary diagnostics on the basis of the dynamic and thermodynamic structures of MJO propagation. These dynamics-oriented diagnostics not only identify models' shortcomings in representing physical processes but also reveal whether models can reproduce the eastward propagation of MJO for the correct dynamical reason. In addition, these diagnostics are easy to compute but objectively measure the fidelity of simulated structure.

With participation from nearly two dozen international climate modeling centers, phase 5 of the Coupled Model Intercomparison Project (CMIP5) (Taylor et al. 2012) provides a useful platform in support of climate model intercomparison, diagnosis, climate change attribution, and projection. Although many efforts have been devoted to assessing MJO simulation, whether CMIP5 models can simulate the eastward propagation of MJO for the correct dynamical reason is not yet clear. Thus, in this study we apply the dynamics-oriented diagnostics to 20 CMIP5 models to evaluate the three-dimensional dynamic and thermodynamic structures of MJOs, which is the key for reproducing the eastward propagation (Wang et al. 2018).

Following this introduction, Section 2 describes the data and method. Section 3 introduces the way in which the propagation of MJO was quantitatively and objectively measured. Section 4 depicts the contrasting MJO structures in two groups of models (those that realistically simulate the eastward propagation and those that do not) and the possible reasons. Finally, a summary of the main findings and a brief discussion are given in Section 5.

2 Data and objective measures

2.1 Data

For observations, daily precipitation data from GPCP (Global Precipitation Climatology Project) (Huffman et al. 2001) for the period 1997–2013 were employed. The ERA-Interim reanalysis daily dataset (Dee et al. 2011), including temperature, horizontal and vertical winds, and specific humidity during 1997–2013, were also used. Twenty-year (1986–2005) integrations from the historical runs of 20 CMIP5 CGCMs (Table 1) were used for evaluation. The simulations provided daily data with eight vertical pressure levels. All the data were interpolated into 2.5° × 2.5° grids for a fair comparison. In the present study, the intraseasonal signal during boreal winter (from November to April) was extracted by a 20- to70-day band-pass filter.

2.2 Objective measures

Two objective measures were employed as metric fields to quantify the performance of models. One was the pattern correlation coefficient (PCC), which was used to gauge the degree of similarity between observed and simulated fields. The other was the domain-averaged normalized root-mean-square error (NRMSE) (Lee and Wang 2014), which was used to measure the magnitude of the simulation error. The NRMSE is the root-mean-square error normalized by the observed standard deviation that is calculated with reference to the whole domain. Note that NRMSE is a much stricter metric than PCC in evaluating the skill of the model. Smaller NRMSE means the model better capture not only the pattern distribution but also the magnitude. Thus, here we use NRMSE for model ranking.

3 Selection of good and poor models

The prominent differences in dynamic and thermodynamic structures of MJO can be revealed by comparing the features of good and poor models. Thus, we firstly distinguished the good and poor models according to their performances with respect to eastward propagation. Following the approach introduced by Wang et al. (2018), we used the 20- to 70-day filtered daily precipitation and averaged precipitation within three reference regions – the equatorial Indian Ocean (EIO; 10°S–10°N, 80°–100°E); the Maritime Continent (MC; 10°S–10°N, 110°–130°E); and the equatorial western Pacific (EWP; 10°S–10°N, 140°–160°E) – to construct the time–longitude lead-lag correlation diagrams, which is a simple but effective way to measure MJO propagation.

Figures 1a–c show time–longitude lead-lag correlation maps with reference to EIO, MC, and EWP rainfall anomalies, respectively. Here, propagation diagrams from observation and two best and two worst models' simulations are displayed for brevity. Clearly, the best two models reproduce the eastward propagation of MJO realistically, while the worst two models are characterized by a largely stationary propagation mode. The NRMSE skills for each model are shown in Fig. 1d, which range from 0.29 to 0.82. The lower NRMSE skills indicate more systematic eastward propagation. It has been suggested that the performance of overall propagation can be better reflected by the averaged skill over three reference regions than that measured by one single reference region (Wang and Lee 2017). Thus, we selected the top four models (hereafter referred to as "good" models) and four poorest models (hereafter referred to as "poor" models) in terms of the averaged NRMSE skills between the observed and simulated propagation diagram regarding rainfall anomalies at three key locations. The longitudinal range between 85°E and 95°E for the EIO, 115°E and 125°E for the MC,

Table 1 Description of the CMIP5 models used in the study

Model designation	Institution	AGCM resolution (lon × lat)
ACCESS1–0	Commonwealth Scientific and Industrial Research Organization and Bureau of Meteorology (CSIRO-BOM), Australia	1.875° × 1.25°
BNU-ESM	College of Global Change and Earth System Science (GCESS), Beijing Normal University (BNU), China	2.8125° × 2.8125°
CanESM2	Canadian Centre for Climate Modelling and Analysis (CCCma), Canada	2.8125° × 2.8125°
CMCC-CESM	Centro Euro-Mediterraneo per I Cambiamenti Climatici (CMCC), Italy	3.75° × 3.75°
CMCC-CMS		1.875° × 1.875°
CNRM-CM5	Centre National de Recherches Meteorologiques/Centre Europeen de Recherche et Formation Avancees en Calcul Scientifique (CNRM-CERFACS), France	1.40625° × 1.40625°
CSIRO-Mk3–6-0	Commonwealth Scientific and Industrial Research Organization and the Queensland Climate Change Centre of Excellence (CSIRO-QCCCE), Australia	1.875° × 1.875 °
FGOALS-g2	LASG, Institute of Atmospheric Physics, Chinese Academy of Sciences; and CESS, Tsinghua University (LASG-CESS), China	2.8125° × 2.8125°
GFDL-CM3	Geophysical Fluid Dynamics Laboratory (NOAA GFDL), USA	2.5° × 2°
GFDL-ESM2M		2.5° × 2°
GFDL-ESM2G		2.5° × 2°
IPSL-CM5A-LR	Institute Pierre-Simon Laplace (IPSL), France	3.75° × 1.875°
IPSL-CM5A-MR		2.5° × 1.258°
IPSL-CM5B-LR		3.75° × 1.875°
MIROC5	Atmosphere and Ocean Research Institute (University of Tokyo), National Institute for Environmental Studies, and Japan Agency for Marine-Earth Science and Technology (MIROC), Japan	1.40625° × 1.40625°
MIROC-ESM-CHEM		2.8125° × 2.8125°
MIROC-ESM		2.8125° × 2.8125°
MPI-ESM-LR	Max Planck Institute for Meteorology (MPI-M), Germany	1.875° × 1.875°
MRI-CGCM3	Meteorological Research Institute (MRI), Japan	1.125° × 2.25°
NorESM1-M	Norwegian Climate Centre (NCC), Norway	1.875° × 1.875°

and 145°E and 155°E for the EWP, and is excluded when NRMSE is calculated. The exclusion at the reference point is because even the poor models have good skill at the reference point, due to local stationary oscillation. The four good (poor) models with realistic (no) MJO eastward propagation are CNRM-CM5, NorESM1-M, GFDL-CM3, and MRI-CGCM3 (IPSL-CM5A-LR, IPSL-CM5A-MR, GFDL-ESM2M, CanESM2). In addition, all models' composite results are also discussed to show the average level of simulation skill of CMIP5 models.

4 Dynamics-oriented diagnostics

In order to examine the dynamic and thermodynamic structures related to MJO propagation for CMIP5 models, we employed the six dynamics-oriented diagnostic metrics developed by Wang et al. (2018), including (1) the low-level (850-hPa) horizontal structure of circulation, (2) the preceding propagation of low-level (850-hPa) moisture convergence, (3) the equatorial vertical longitudinal structure of the equivalent potential temperature (EPT), (4) the equatorial vertical longitudinal distribution of diabatic heating, (5) the available potential energy (APE) generation of MJO, and (6) the upper-level diabatic heating and divergence. Note that all regressed MJO dynamic and thermodynamic anomalies were calculated against the rainfall anomalies only over the EIO, because the rainfall and circulation of MJO over the EIO are less affected by the mean flow, and it is more equatorially symmetric (Wang and Lee 2017).

4.1 Low-level (850-hPa) horizontal circulation

It has been revealed that MJO eastward propagation performances are robustly correlated with its low-level horizontal circulation structure (Wang and Lee 2017). Figure 2a shows that the observed 850-hPa circulation anomaly has an equatorial Rossby wave component to the west of the EIO center and an equatorial Kelvin wave component to the east of it. Opposite to the Gill pattern (Gill 1980), the maximum Rossby westerly wind speed is smaller than the maximum Kelvin easterly wind speed for MJO low-level circulation (Wang and Lee 2017). The different structure may result from the nature of the heating (Wang et al. 2018; Wang and Lee 2017): the heating is interactive with the circulation of MJO, while the heating is specified and the waves are a passive response in the Gill model. The intensity and zonal extent of the equatorial Rossby westerly versus Kelvin easterly are the obvious differences between the

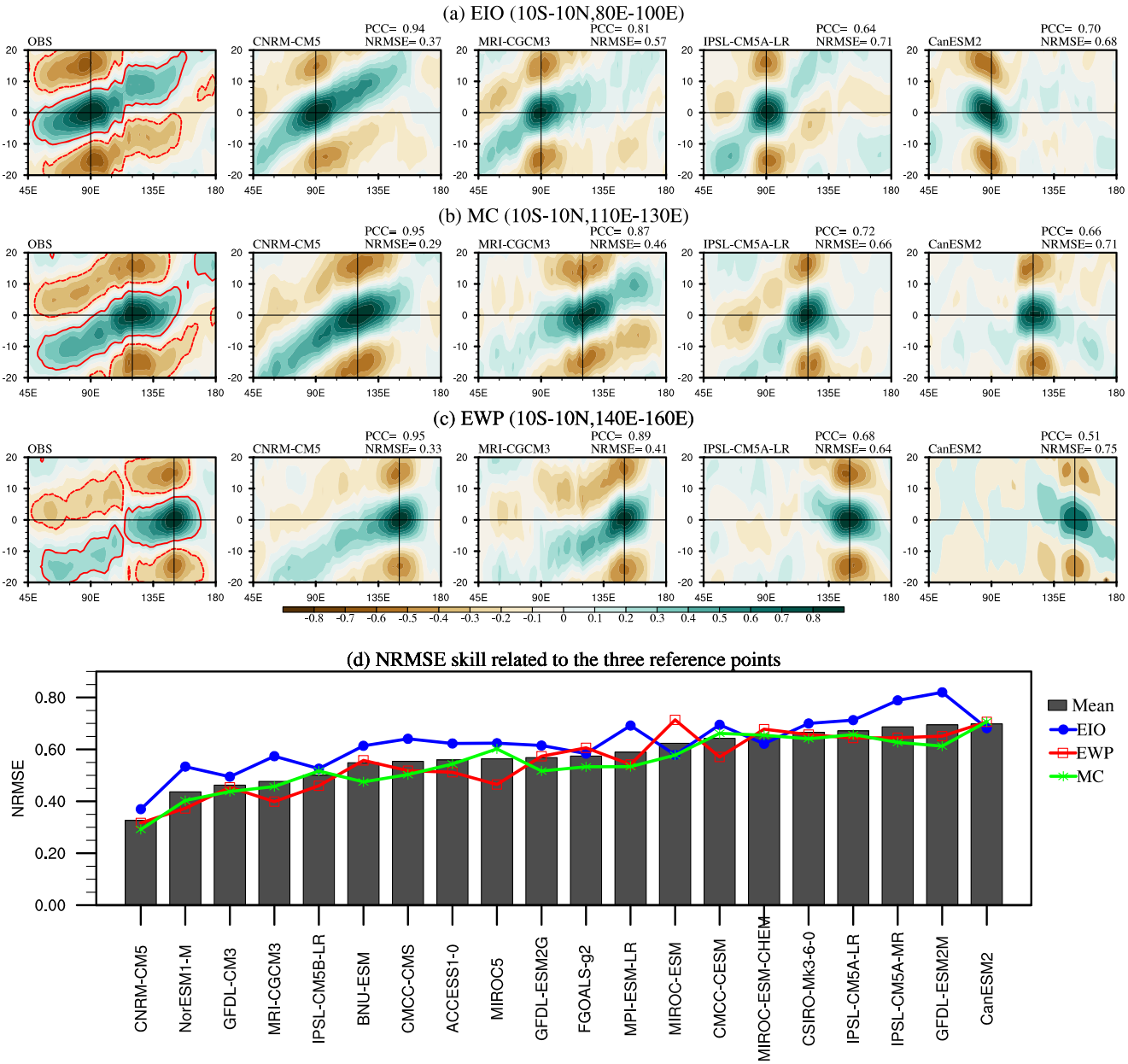

Fig. 1 Time-longitude diagram of 10°N–10°S-averaged 20- to 70-day band-pass-filtered precipitation anomalies correlated with precipitation anomalies averaged over the **a** Equatorial Indian Ocean (EIO; 10°S–10°N, 80°–100°E), **b** Maritime Continent (MC; 10°S–10°N, 110°–130°E), and **c** equatorial western Pacific (EWP; 10°S–10°N, 140°–160°E) during boreal winter (November–April). **d** The NRMSE skill of 20 CMIP5 model simulations related to the three reference points. The PCC/NRMSE skill is calculated where the absolute value of the correlation coefficient is greater than 0.2 in the domains outlined by red curves within 50°E–180° from day (− 20) to day(+ 20); and the longitudinal ranges between 85°E and 95°E for the EIO, between 115°E and 125°E for the MC, between 145°E and 155°E for the EWP are excluded in the calculation of the PCC/NRMSE

good and poor models (Figs. 2b, c). For good models, the maximum Rossby westerly is weaker than the maximum Kelvin easterly, which resembles the observed MJO structure; whereas, for poor models, the maximum Kelvin easterly is weaker than the maximum Rossby westerly, which resembles the Gill pattern. It is suggested that a model's cumulus parameterization scheme, which may give rise to different interaction between dynamics of equatorial wave and convective heating (Wang et al. 2016), is one of the key factors for the performance in simulating the horizontal structures of MJO. About three quarters of models have PCC larger than 0.7 and NRMSE less than 1.0, indicating that most models can well simulate the low-level circulation structure of MJO, which is also implied by the composite structures from all models (Fig. 2d).

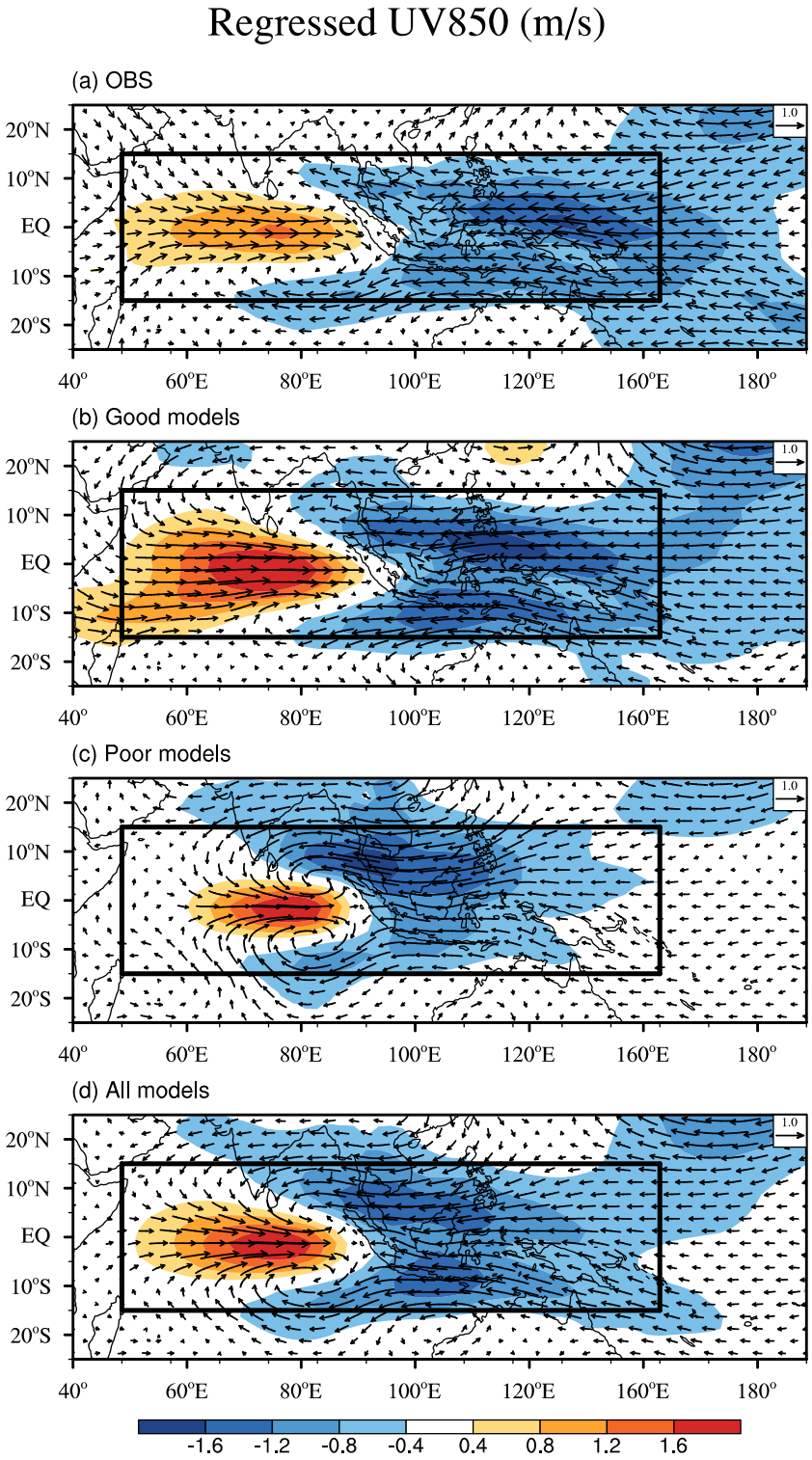

Fig. 2 Horizontal structure of 20- to 70-day band-pass-filtered 850-hPa wind (m s^{-1}, vectors) and 850-hPa zonal wind speed (U850) (m s^{-1}, shading) regressed onto 20- to 70-day band-pass-filtered precipitation over the Indian Ocean (10°S–10°N, 80°–100°E) during boreal winter (November–April) for **a** observations, **b** the composite of good model simulations, **c** the composite of poor model simulations, **d** the composite of all 20 model simulations. The regression strengths are scaled to a fixed 3 mm day^{-1} precipitation rate

4.2 Propagation of low-level (850-hPa) moisture convergence

It has been suggested that the boundary layer moisture convergence (BLMC) couples Rossby and Kelvin waves as well as convection together (Wang et al. 2016), favoring the eastward propagation of MJO by pre-moistening, pre-destabilization, generating APE, and heating in the lower troposphere to the east of the convective center (Wang and Lee 2017). Thus, the evolution of the equatorial BLMC is examined as in Fig. 3. The observed eastward propagation of BLMC from 50°E to 180° is significant in good model simulations

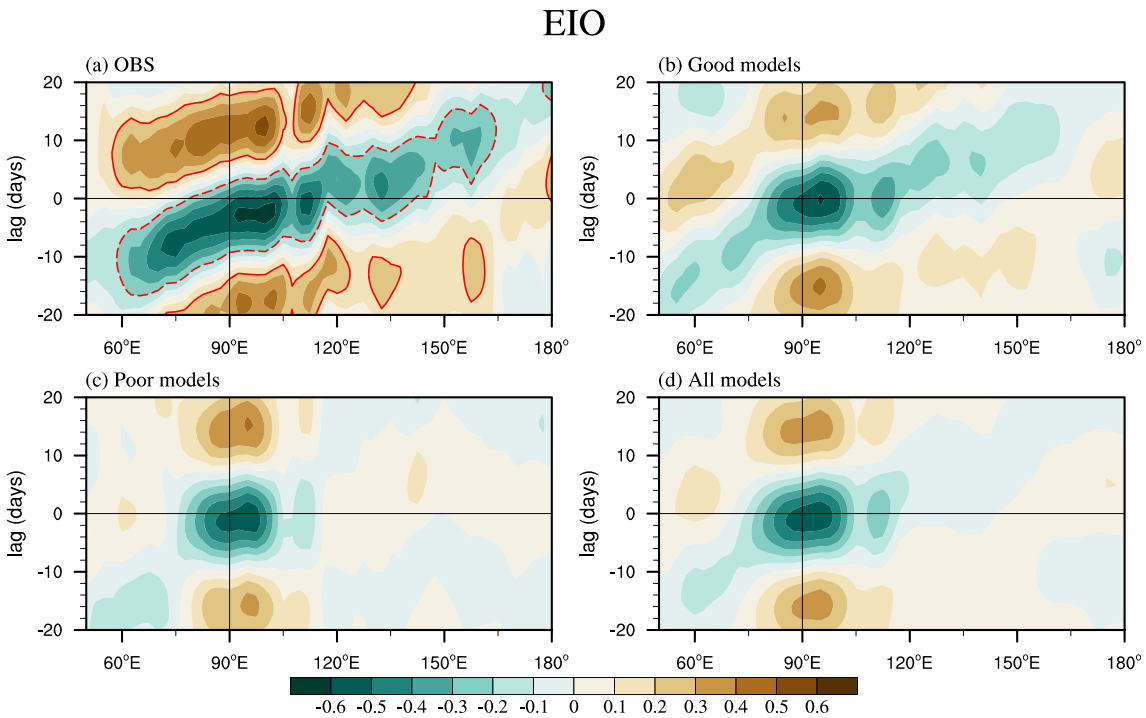

Fig. 3 Time–longitude diagram of 5°N–5°S-averaged 20- to 70-day band-pass-filtered 850-hPa moisture divergence anomalies correlated with precipitation anomalies averaged over the Equatorial Indian Ocean (EIO; 10°S–10°N, 80°–100°E) during boreal winter (November–April) for **a** observations, **b** the composite of good model simulations, **c** the composite of poor model simulations, and **d** the composite of all 20 model simulations

(Fig. 3b), while no propagation can be seen in the poor models (Fig. 3c). Previous studies have revealed that BLMC propagation leads propagation of rainfall by about 5 days in observations (Wang and Lee 2017; Wang et al. 2018), implying the BLMC is an indicator of MJO eastward propagation. In comparison with Fig. 1a, this phase-leading is about 2 days in the simulation of good models but is not found in that of poor models. In other words, failure in simulating the eastward propagation of BLMC and the phase-leading is one of the reasons that poor models have difficulties in simulating MJO eastward propagation. These models may have problems in representing boundary layer convergence and its interaction. The eastward propagation of BLMC shows a near-stationary mode in the composite results from all models (Fig. 3d), suggesting that simulating the propagation of BLMC may be a common problem in CMIP5 models.

4.3 Vertical structure of equivalent potential temperature

Another important indicator for the eastward propagation of MJO is the rearward-tilted structure of the lower-tropospheric EPT (Hsu and Li 2012; Wang et al. 2018). The vertical structure of the EPT (Fig. 4a) confirms this observed thermodynamic feature. It is found that the maximum EPT is at 500 hPa, and westward and upward tilt of the EPT is obvious below the 500-hPa level. The rearward-tilted structure reflects the westward gradual thickening of the humid layer on the east side of the deep convective center of MJO, suggesting pre-moistening and pre-destabilization processes preceding MJO deep convection. Both the good and poor models reproduce the maximum EPT at 500 hPa. The prominent difference between their composite results is that the rearward-tilted structure between 120°E and 150°E below the 500-hPa level is only found in the good models (Figs. 4b, c). This means that the poor models fail to simulate the pre-moistening and pre-destabilization processes to the east of MJO convection, suggesting problems regarding the shallow-congestus clouds and BLMC interaction through low-cloud feedback and convective mixing in the lower troposphere (Wang et al. 2018). About two thirds of models have PCC larger than 0.7 and NRMSE smaller than 1.0, indicating that the majority of models can simulate the tilted structure. This is also indicated by the composite from all models that shows a tilted structure extended to 135°E (Fig. 4d).

4.4 Vertical structure of diabatic heating

The diabatic heating of MJO is associated with the transition of clouds from shallow cumuli, to congestus, to deep convective and stratiform clouds (Jiang et al. 2011; Sperber 2003; Wang et al. 2018). The observed

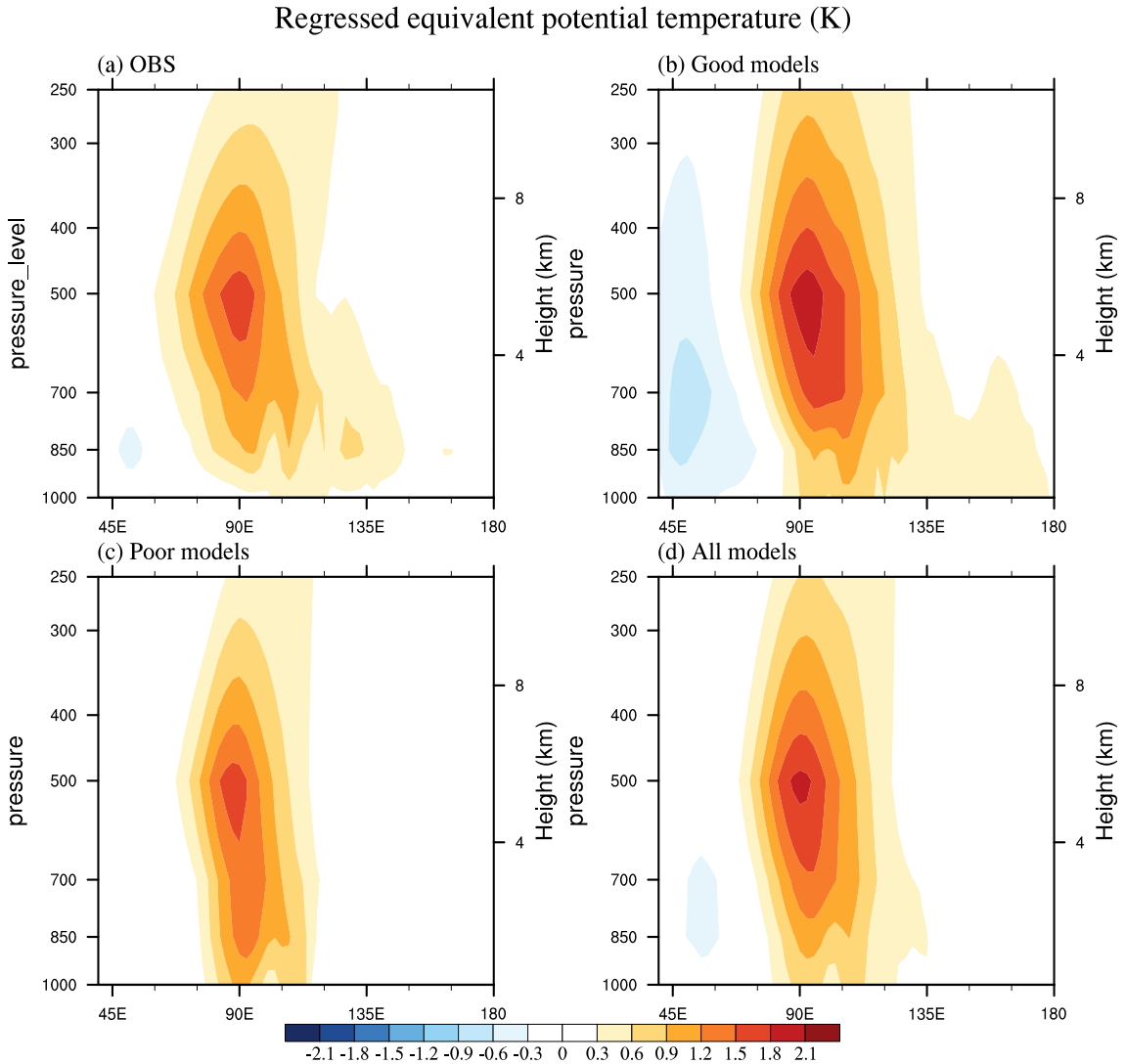

Fig. 4 Vertical structure of regressed 20- to 70-day band-pass-filtered equivalent potential temperature (K, averaged over 5°S–5°N) with reference to the precipitation anomaly in the equatorial Indian Ocean averaged over (10°S–10°N, 80°–100°E) during boreal winter (November–April) for **a** observations, **b** the composite of good model simulations, **c** the composite of poor model simulations, and **d** the composite of all 20 model simulations. The regression strengths are scaled to a fixed 3 mm day^{-1} precipitation rate

equatorial longitudinal distribution of the diabatic heating of MJO shows a vertical rearward-tilted structure (Fig. 5a), reflecting the transition of the cloud types. The lower-tropospheric heating leads the mid-tropospheric deep convection heating that is then followed by upper-tropospheric heating expanding from the deep convection center to 60°E. The lower-tropospheric diabatic heating suggests that the existence of shallow-congestus clouds may lead the deep convective cloud, while the upper-tropospheric heating indicates that the stratiform cloud may follow the deep convective cloud. The good models simulate a realistic vertically tilted structure of diabatic heating, whereas the poor models fail to capture it (Figs. 5b, c). In the poor models, no lower-tropospheric diabatic heating can be found leading deep convection, and the upper-tropospheric heating does not extend westward. The failure to simulate this diabatic heating structure may relate to the representation of cloud and scheme of cumulus parameterization in the CGCMs (Ma et al. 2019). For the composite from all models (Fig. 5d), although the leading diabatic heating can be seen, the signal of the westward extension of the upper-tropospheric heating is unclear.

4.5 MJO available potential energy generation

One of the sources of energy for MJO development is an eddy APE (Wang et al. 2018). Therefore, the vertical structures of eddy APE generation are examined.

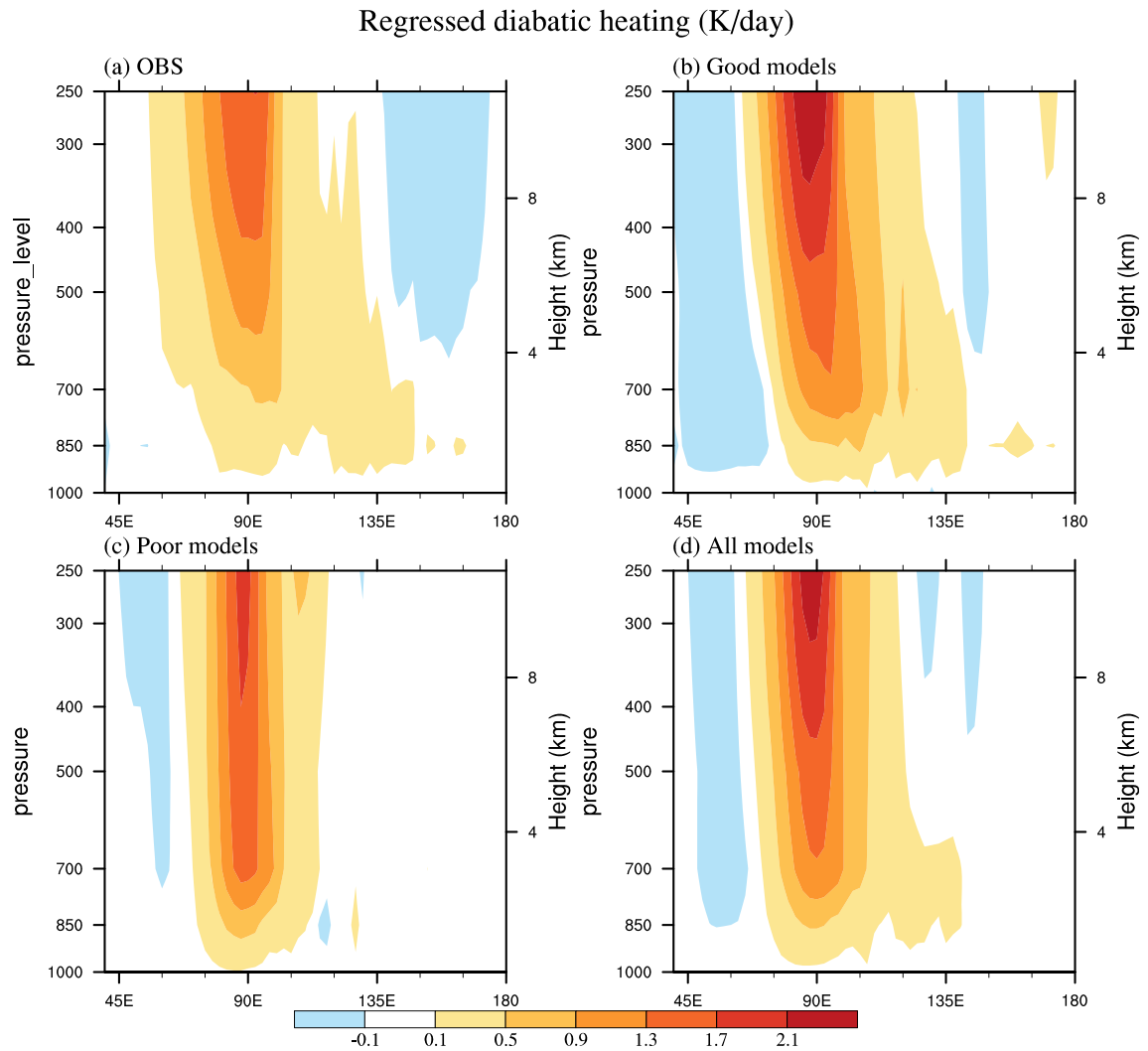

Fig. 5 As in Fig. 4, but for diabatic heating (K day^{-1}, shading)

Figure 6 displays the vertical–longitudinal profile of the MJO APE generation rate. Note that larger amplitude of observed APE generation is found to the east of MJO convective center than that to the west of the convective center (Fig. 6a). This zonal asymmetry of observed APE generation is significant in the lower troposphere (Fig. 6a). The generation of APE over the convective center mainly serves to amplify the MJO. Meanwhile, the eastward propagation of the MJO is facilitated by more generation of APE to the east of 90°E through converting the APE to kinetic energy of MJO. As shown in Fig. 6b and c, in the good models, more generation of APE appears to the east of MJO convective center in the lower troposphere, while in the poor models, it is quasi-symmetric. This zonal asymmetry in APE generation is largely caused by the positive temperature anomalies and the heating to the east of the 90°E in the lower troposphere (Wang et al. 2018), which plays a vital role for CGCMs in reproducing the zonal asymmetry of APE generation. As shown in Fig. 6d, APE generation is not observed in the lower troposphere, indicating that most models have difficulties in capturing the zonal asymmetry of APE generation.

4.6 Upper-level (250-hPa) divergence and diabatic heating

Another good indicator of MJO eastward propagation is the upper-level divergence (Adames and Wallace 2015), which reflects the upper-level precipitation heating. Figure 7a shows the observed 250-hPa winds and associated divergence regressed on EIO precipitation. The upper-level circulation is characterized by equatorial Rossby easterlies to the west of the EIO and equatorial Kelvin westerlies to the east of the EIO (Fig. 7a), which

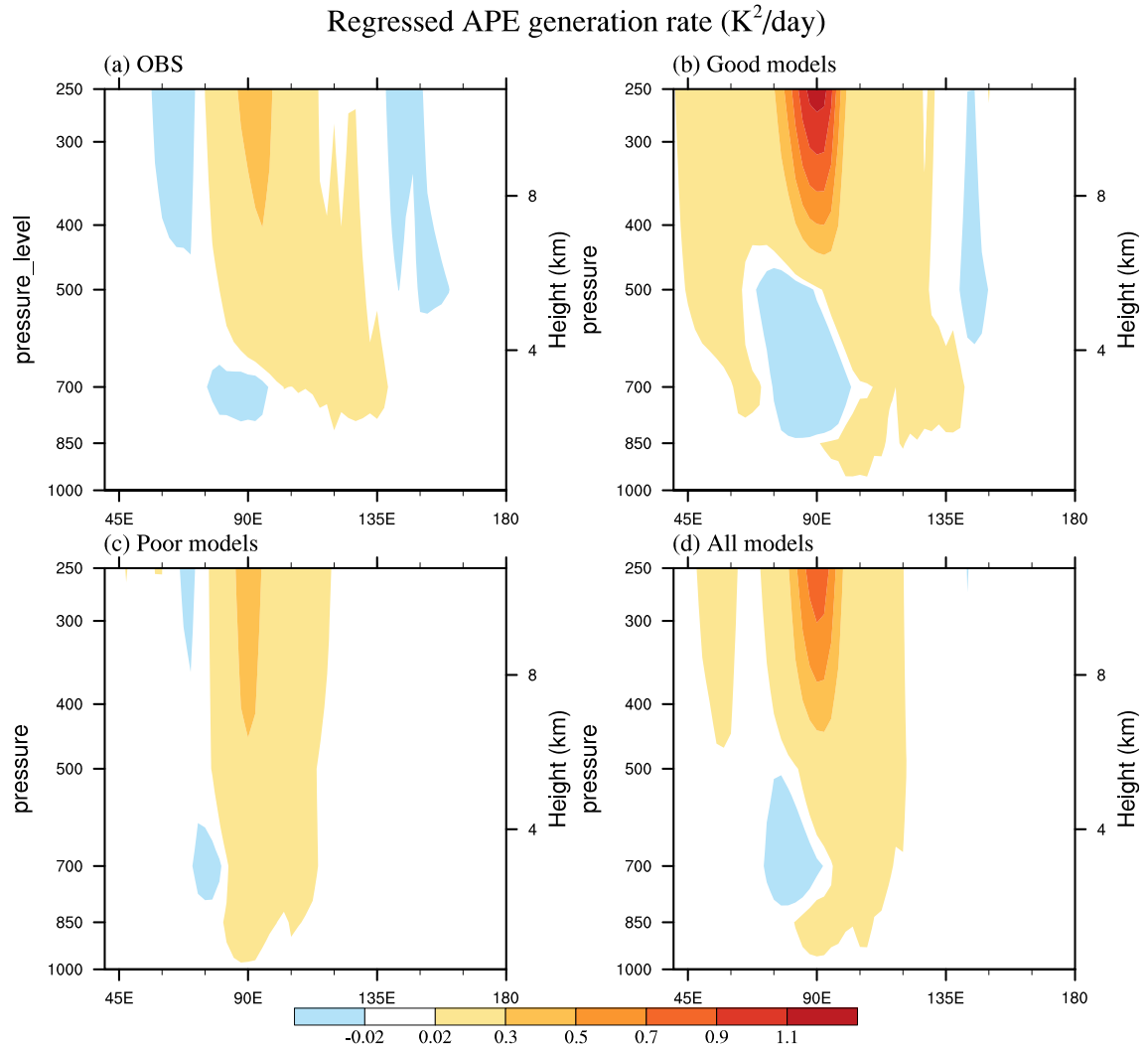

Fig. 6 As in Fig. 4, but for the eddy available potential energy (APE) generation rate (K^2 day^{-1})

is approximately opposite to that at 850 hPa (Fig. 2a). It is obvious that the Kelvin westerly anomalies are much weaker than the Rossby wave easterly anomalies, which is out of phase with the zonal asymmetry in the 850-hPa zonal wind speed (U850) results. The 250-hPa divergence center overlays the convective region and extends westward to the western Indian Ocean. It suggests that the westward extension of diabatic heating generated by stratiform clouds is the primary reason that results in the westward extension of the 250-hPa divergence. These characteristics in observation are well simulated by the good models (Fig. 7b). However, in the poor-models or all-models composite results, the zonal asymmetry in 200-hPa wind is opposite to that in observations; plus, the divergence and diabatic heating does not extend westward to the western Indian Ocean (Figs. 7c, d). These deficiencies might be related to the models' capability in simulating the congestus and stratiform cloud (Kim and Seo 2018).

5 Summary

MJO dynamics-oriented diagnostics (Wang et al. 2018) are applied to 20 CMIP5 CGCMs' simulation in this study. These diagnostics are focused on the MJO's fundamental dynamic and thermodynamic characteristics that are essential to its eastward propagation. Generally, good models with realistic MJO propagation show the following features that resemble observations: (1) the weaker intensity and smaller zonal extent of the equatorial Rossby westerly versus Kelvin easterly at the low level; (2) a preceding eastward propagation of BLMC, which leads the propagation of convection; (3) a rearward-tilted vertical structure of EPT, which reflects processes of pre-moistening and pre-destabilization; (4) a rearward-tilted vertical structure of diabatic heating, which reflects the clouds transition; (5) APE generation, which amplifies MJO intensity and facilitates the

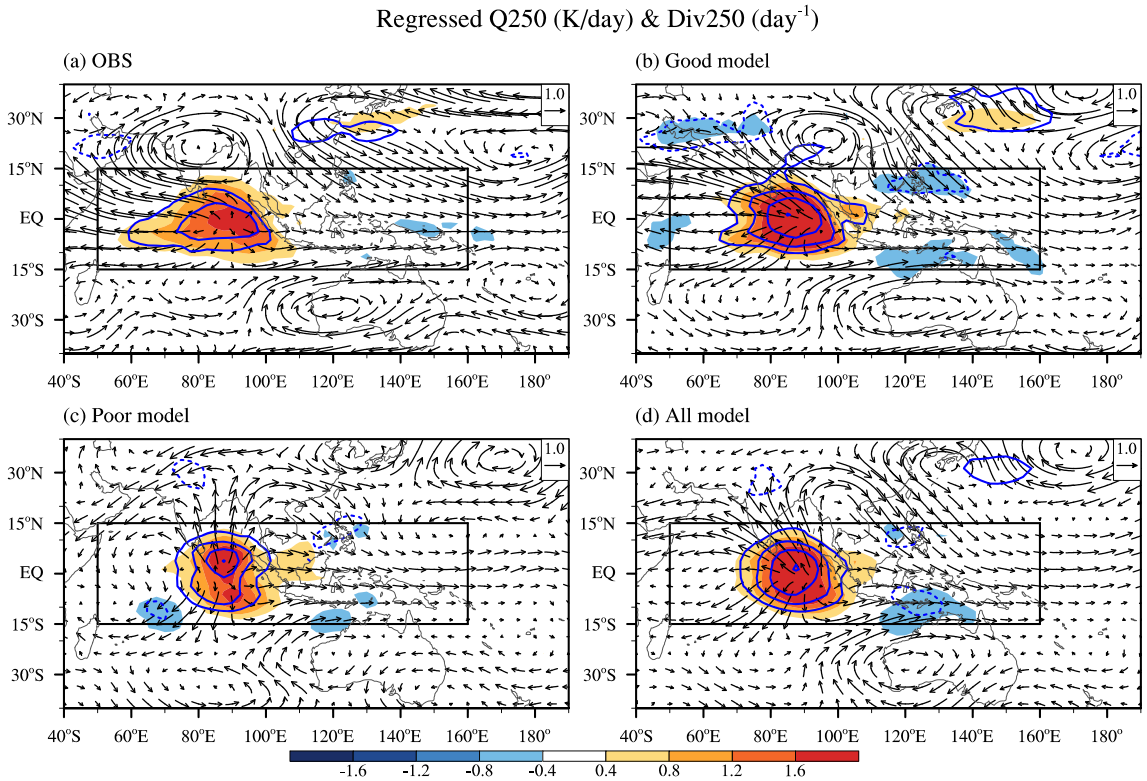

Fig. 7 Horizontal structure of 20- to 70-day band-pass-filtered 250-hPa wind (m s^{-1}, vectors), 250-hPa divergence (day^{-1}, contours), and 250-hPa diabatic heating (K day^{-1}, shading) regressed onto 20- to 70-day band-pass-filtered precipitation over the Indian Ocean (10°S–10°N, 80°–100°E) during boreal winter (November–April) for **a** observations, **b** the composite of good model simulations, **c** the composite of poor model simulations, and **d** the composite of all 20 model simulations. The regression strengths are scaled to a fixed 3 mm day^{-1} precipitation rate

eastward propagation of MJO; and (6) zonal asymmetry in the upper-level divergence and diabatic heating, which indicates the formation of stratiform clouds. Conversely, the poor models fail to simulate these structures and the eastward propagation of MJO. The potential sources of the shortcomings have been discussed, highlighting the representation of clouds and parameterization in models as playing a key role.

Figure 8 summarizes the performance skills of each individual model in simulating the dynamic and thermodynamic structures of MJO investigated in this study. The individual CMIP5 models have PCCs (NRMSEs) ranging from 0.56 to 0.97 (0.57 to 1.37) for the horizontal structure of U850; 0.33 to 0.90 (0.45 to 0.94) for the propagation of BLMC; 0.62 to 0.85 (0.63 to 1.27) for the vertical structure of EPT; 0.46 to 0.87 (0.71 to 1.84) for the vertical structure of diabatic heating; 0.34 to 0.88 (0.77 to 5.26) for the vertical structure of APE generation; 0.58 to 0.88 (0.77 to 1.50) for the horizontal structure of divergence at 250 hPa; and 0.62 to 0.89 (0.65 to 1.29) for the horizontal structure of diabatic heating at 250 hPa. Compared to the reference skills from the simulations of 24 GCM [Table 3 in Wang et al. 2018], approximately 25% to 40% of CMIP5 models can be considered "good" models in simulating the seven diagnostic fields. In other words, more than half of CMIP5 models still have difficulties regarding these dynamic/thermodynamic structures, resulting in failure to simulate MJO eastward propagation. Note that CNRM-CM5, which is one of the best models at reproducing MJO eastward propagation, has low skill in simulating the vertical structure of APE (PCC = 0.54, NRMSE = 5.26). This large bias is mainly due to an overestimation of diabatic heating in the upper troposphere and underestimation of the temperature anomalies in the lower troposphere over the major convective center.

Through diagnoses such as these, we provide a better chance of understanding what model processes require improvement. It may also be possible to gain confidence that subsets of models are more reliable for investigating MJO, which may be a better choice for forecasting. The possible reasons behind the performance of models have been discussed, which will hopefully shed some light on ways to reduce model biases. However, sensitivity experiments are needed to be conducted in the future to test these possible reasons.

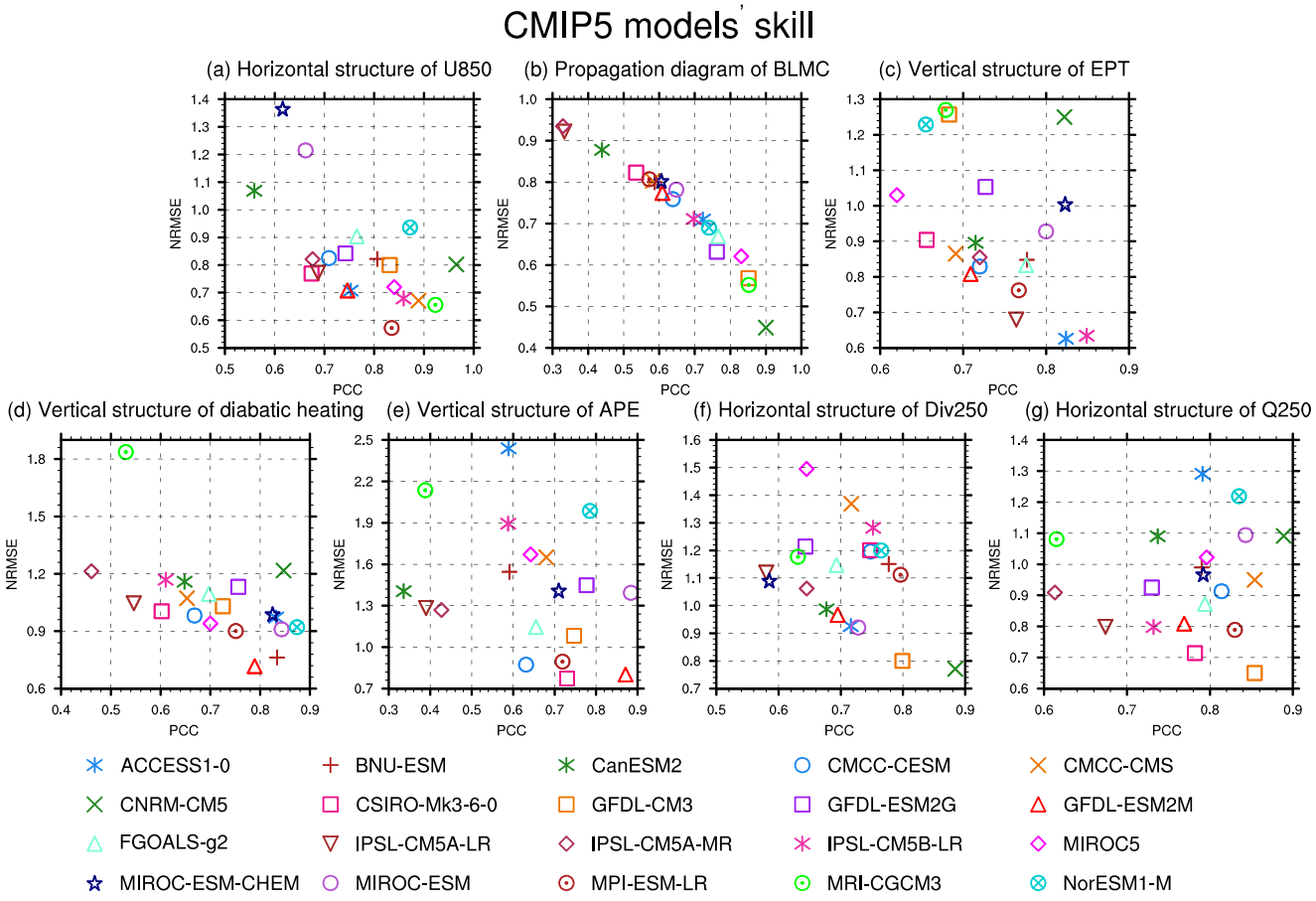

Fig. 8 The PCC and NRMSE skills of 20 CMIP5 model simulations for **a** the horizontal structure of 850-hPa zonal wind; **b** the propagation diagram of 850-hPa boundary layer moisture convergence (BLMC); **c** the vertical structure of equivalent potential temperature (EPT); **d** the vertical structure of diabatic heating; **e** the vertical structure of the eddy available potential energy (APE) generation rate; **f** the horizontal structure of 250-hPa divergence (Div250); **g** the horizontal structure of 250-hPa diabatic heating. The PCC and NRMSE skills for horizontal structures (Figs. 8a–g) are calculated over (15°S–15°N, 50°–160°E) (black rectangle in Fig. 2 and Fig. 7). The longitudinal range between 85°E and 95°E is excluded in the calculation of PCC and NRMSE for vertical structure (Figs. 8c–e). For (b), the PCC and NRMSE skills are calculated where the absolute value of the correlation coefficient is greater than 0.2 in the domains outlined by red curves in Fig. 3a; and the longitudinal range between 85°E and 95°E is excluded in the calculation of the PCC and NRMSE

Funding information This work was supported by the National Key R&D Program of China (Grant No. 2018YFC1505905) and the National Natural Science Foundation of China (Grant No. 41805048, Grant No. 41605035). ZW Zhu is supported by the Young Elite Scientists Sponsorship Program by CAST (Grant no. 2018QNRC001).

References

Adames ÁF, Wallace JM (2015) Three-dimensional structure and evolution of the moisture field in the MJO. J Atmos Sci 72:3733–3754

Ahn MS et al (2017) MJO simulation in CMIP5 climate models: MJO skill metrics and process-oriented diagnosis. Clim Dyn 49:4023–4045

Bhatla R, Singh M, Pattanaik DR (2017) Impact of Madden-Julian oscillation on onset of summer monsoon over India. Theor Appl Climatol 128:381–391

Christophe C (2008) Intraseasonal interaction between the Madden-Julian oscillation and the North Atlantic oscillation. Nature 455: 523–527

Dee DP et al (2011) The ERA-interim reanalysis: configuration and performance of the data assimilation system. Q J R Meteorol Soc 137: 553–597

Ferranti L, Palmer TN, Molteni F, Klinker E (1990) Tropical-extratropical interaction associated with the 30–60 day oscillation and its impact on medium and extended range prediction. J Atmos Sci 47:2177–2199

Gill AE (1980) Some simple solutions for heat-induced tropical circulation. Q J R Meteorol Soc 106:447–462

Hai L, Brunet G, Derome J (2009) An observed connection between the North Atlantic oscillation and the Madden-Julian oscillation. J Clim 22:364–380

Hall JD, Matthews AJ, Karoly DJ (2001) The modulation of tropical cyclone activity in the Australian region by the Madden–Julian oscillation. Mon Weather Rev 129:2970–2982

Ho C-H, Kim J-H, Jeong J-H, Kim H-S, Chen D (2006) Variation of tropical cyclone activity in the South Indian Ocean: El Niño–Southern oscillation and Madden-Julian oscillation effects. J Geophys Res Atmos 111

Hsu PC, Li T (2012) Role of the boundary layer moisture asymmetry in causing the eastward propagation of the Madden–Julian oscillation. J Clim 25:4914–4931

Huffman GJ et al (2001) Global precipitation at one-degree daily resolution from multisatellite observations. J Hydrometeorol 2:36–50
Hung MP et al (2013) MJO and convectively coupled equatorial waves simulated by CMIP5 climate models. J Clim 26:6185–6214
Jiang X et al (2011) Vertical diabatic heating structure of the MJO: intercomparison between recent reanalyses and TRMM estimates. Mon Weather Rev 139:3208–3223
Jiang X, Zhao M, Waliser DE (2012) Modulation of tropical cyclones over the eastern Pacific by the intraseasonal variability simulated in an AGCM. J Clim 25:6524–6538
Jiang X et al (2015) Vertical structure and physical processes of the Madden-Julian oscillation: exploring key model physics in climate simulations. J Geophys Res Atmos 120:4718–4748
Jones C (2000) Occurrence of extreme precipitation events in California and relationships with the Madden–Julian oscillation. J Clim 13: 3576–3587
Kim GU, Seo KH (2018) Identifying a key physical factor sensitive to the performance of madden–Julian oscillation simulation in climate models. Clim Dyn 50:391–401
Kim D et al (2009) Application of MJO simulation diagnostics to climate models. J Clim 22:6413–6436
Lee J-Y, Wang B (2014) Future change of global monsoon in the CMIP5. Clim Dyn 42:101–119
Liu P et al (2009) Tropical intraseasonal variability in the MRI-20km60L AGCM*. J Clim 22:2006–2022
Ma L et al (2019) Revisiting the impact of stochastic multicloud model on the MJO using low-resolution ECHAM6.3 atmosphere model. J Meteorol Soc Jpn Ser II 97:977–993
Singh SV, Kripalani RH, Sikka DR (1992) Interannual variability of the Madden-Julian oscillations in Indian summer monsoon rainfall. J Clim 5:973–978
Slingo JM, Rowell DP, Sperber KR, Nortley F (1999) On the predictability of the interannual behaviour of the Madden-Julian oscillation and its relationship with El Niño. Q J R Meteorol Soc 125:583–609
Sperber KR (2003) Propagation and the vertical structure of the Madden–Julian oscillation. Mon Weather Rev 131:3018–3037
Sperber KR (2004) Madden-Julian variability in NCAR CAM2.0 and CCSM2.0. Clim Dyn 23:259–278
Stewart J (2009) Implication of the Madden–Julian oscillation in the 40-day variability of the West African monsoon. J Clim 22:3769–3785
Taylor KE, Stouffer RJ, Meehl GA (2012) An overview of CMIP5 and the experiment design. B Am Meteorol Soc 93:485–498
Waliser D et al (2009) MJO simulation diagnostics. J Clim 22:3006–3030
Wang B, Ding Y (1992) An overview of the Madden-Julian oscillation and its relation to monsoon and mid-latitude circulation. Adv Atmos Sci 9:93–111
Wang B, Lee SS (2017) MJO propagation shaped by zonal asymmetric structures: results from 24 GCM simulations. J Clim 30:7933–7952
Wang B, Liu F, Chen G (2016) A trio-interaction theory for Madden–Julian oscillation. Geosci Lett 3:34
Wang B et al (2018) Dynamics-oriented diagnostics for the Madden–Julian oscillation. J Clim 31:3117–3135
Wheeler MC, Hendon HH, Cleland S, Meinke H, Donald A (2009) Impacts of the Madden–Julian oscillation on Australian rainfall and circulation. J Clim 22:1482–1498
Yang Y, Zhu Z, Li T, Yao M (2020) Effects of the western Pacific intraseasonal convection on the surface air temperature anomalies over North America. Int J Climatol 40:2913–2923
Yoo C, Lee S, Feldstein SB (2012) Mechanisms of Arctic surface air temperature change in response to the Madden-Julian oscillation. J Clim 25:5777–5790
Zhou S, L'Heureux M, Weaver S, Kumar A (2012) A composite study of the MJO influence on the surface air temperature and precipitation over the continental United States. Clim Dyn 38:1459–1471